



Adjusting Residual Stresses During Cold Spray Deposition of IN718

J. Schmitt¹ · J. Fiebig¹ · S. Schröder² · O. Guillon^{1,3} · R. Vaßen^{1,4}

Submitted: 31 May 2023 / in revised form: 15 September 2023 / Accepted: 25 September 2023 / Published online: 31 October 2023
 © The Author(s) 2023

Abstract The residual stress state in cold spray coatings, which is typically compressive in nature, can be crucial for the coating integrity at high levels or for thick coatings. As an alternative, the analysis using the curvature measurement was applied in this study. The stress measurement during cold spray deposition was made by using an in situ coating property sensor (ICP sensor), which is relatively widely used in thermal spray and enables a fast comparison of several process parameters. The results were then compared to post-deposition curvature measurements. It could be revealed that the usage of a very slow robot traverse speed can lead to tensile residual stresses in cold-sprayed coatings. This finding was explained by the high local temperature during deposition and the formation of tensile stresses during cooling of the deposited material to the average substrate temperature. The increase in the powder feed rate can increase this effect. Preheating did not influence the final stress state. An analytical model is presented which can at least semi-quantitatively explain the observed findings. As an outcome of the research work, it is now possible to adjust the residual stress state in cold

spray coatings from tensile to compressive and vice versa with the opportunity of a zero stress state.

Keywords analytical model · cold spray · curvature · ICP sensor · Inconel 718 · residual stress

List of Symbols

ASI	Adiabatic shear instability
APS	Atmospheric plasma spray
CGS	Cold gas spray
CTE	Coefficient of thermal expansion
DE	Deposition efficiency
DS	Deposition stresses
HVOF	High-velocity oxide fuel
ICP	In situ coating properties sensor
IN718	INconel 718
PS	Peening stresses
QS	Quenching stresses
TDS	Thermal deposition stresses
TS	Thermal stresses
$\alpha_c [10^{-6} \text{ K}^{-1}]$	Coefficient of thermal expansion, coating
$\alpha_s [10^{-6} \text{ K}^{-1}]$	Coefficient of thermal expansion, substrate
$E_c [\text{MPa}]$	Young's modulus, coating
$E_s [\text{MPa}]$	Young's modulus, substrate
$\kappa [\text{m}^{-1}]$	Curvature
$r [\text{m}]$	Radius of the fitted circle
$v_r [\text{mm s}^{-1}]$	Robot traverse speed
$\nu_c [-]$	Poisson's ratio, coating
$\nu_s [-]$	Poisson's ratio, substrate
$T_m [\text{K}]$	Melting temperature
$T_s [\text{K}]$	Substrate temperature
$T_{s,\text{max}} [\text{K}]$	Substrate temperature (pyrometer)
$T_{\text{th}} [\text{K}]$	Substrate temperature on the rear side

✉ J. Schmitt
 jo.schmitt@fz-juelich.de

¹ Institute of Energy and Climate Research, Materials Synthesis and Processing (IEK-1), Forschungszentrum Jülich GmbH, 52425 Jülich, Germany

² Rolls-Royce Deutschland Ltd & Co KG., 15827 Blankenfelde-Mahlow, Germany

³ Jülich Aachen Research Alliance: JARA-Energy, 52425 Jülich, Germany

⁴ Institut für Werkstoffe, Ruhr-Universität Bochum, Bochum, Germany

T_0 [K]	Room temperature
t_c [mm]	Thickness, coating
t_s [mm]	Thickness, substrate
z [–]	No. of coating cycles
σ_{St} [MPa]	Residual stress from Stoney
σ_{Br} [MPa]	Residual stress from Brenner–Senderoff
b [m]	Meander width
$c_{p,c}$ [J kg ^{−1} K ^{−1}]	Heat capacity, coating
$c_{p,s}$ [J kg ^{−1} K ^{−1}]	Heat capacity, substrate
D_{diff} [m ² s ^{−1}]	Coefficient of thermal diffusion
d_{diff} [m]	Diffusion length scale
d_u [m]	Diameter of the gas spot
e [W m ^{−2} K ^{−1} s ^{−0.5}]	Thermal effusivity
h_g [W m ^{−2} K ^{−1}]	Heat transfer coefficient, gas
T_{loc} [K]	Local temperature at the impact zone
β [W m ^{−2} K ^{−1}]	Heat transfer coefficient, particle
β_0 [W m ^{−4}]	Pre-factor
β_{en} [W m ^{−1} K ^{−1}]	Energy per deposited layer
λ_s [W m ^{−1} K ^{−1}]	Thermal conductivity, substrate
ρ_c [kg m ^{−3}]	Density, coating
ρ_s [kg m ^{−3}]	Density, substrate
τ_{diff} [s]	Time scale for heat diffusion

Introduction

The cold gas spray process (CGS) is a relatively new thermal spray technology introduced 1980 in Novosibirsk (Ref 1). The lower operating temperatures compared with other conventional thermal spray methods make CGS suitable as alternative repair process for materials sensitive to oxidation and further phase transformation (Ref 2–6). A powder used as feedstock material is injected into a process gas jet typically made of nitrogen or helium. This is pre-heated through an elongated pre-chamber. Reaching a subsequent de-Laval nozzle, the particles are accelerated in the high-pressure supersonic gas jet, reaching velocities of 300–1200 m/s. While hitting the substrate at a certain distance to the nozzle exits, the particles are deformed and create a coating due to the bonding process of adiabatic shear instability (ASI), which is widely accepted as bonding mechanism in CGS (Ref 7, 8). Nevertheless, the bonding mechanism is not fully clarified. Hassani-Granaraj postulated that adiabatic shear instability is not necessary for the bonding on CGS (Ref 9). Other models propose bonding as a result of mechanical interlocking due to the out-flowing jet of material at the interface upon particle impact (Ref 10) or material mixing at the interface (Ref 11). The quality of bonding is high in the so-called “Window of Deposition.” In this operational window, the lower particle velocity (v_{crit}) is needed for a successful

bonding while an upper limit indicates dominating erosion effects without bonding (Ref 12, 13). The impact velocity of the particles is affected by the bow shock, created in between the supersonic jet and the substrate (Ref 14). Other publications concerning standoff distance and spray angle of the nozzle revealed a crucial impact of the normal velocity on the resulting deposition efficiency (DE) in CGS coatings (Ref 15, 16).

CGS coatings should have a good adhesion to the substrate and a high density. The adhesion strength can be influenced by the residual stress state during deposition (Ref 17–20). In general, the impact of solid particles at high velocity on the substrate leads to so-called peening stresses (PS), which are compressive in nature and typically dominant in CGS coatings. These compressive stresses enable possible advantages compared to other thermal spray coatings with tensile residual stresses regarding fatigue life or crack development (Ref 18). Tensile residual stresses arise due to the quenching of high-temperature particles on a substrate at lower temperature. These, also called quenching stresses (QS), are known to be dominant in high-temperature thermal spray processes such as atmospheric plasma spray (APS) or high-velocity oxide fuel (HVOF) (Ref 20–23). The value of the stress levels can be estimated for a thin coating using the following equation (Ref 24):

$$\sigma_q = E_c \alpha_c (T_m - T_s) \quad (\text{Eq 1})$$

where E_c and α_c are the Young’s modulus and coefficient of thermal expansion of the coating, respectively, T_m is the melting temperature of the coating material, and T_s is the temperature of the substrate during deposition. However, the results typically in the GPa range lead to relaxation of the coatings, often by crack formation or plastic deformation.

Furthermore, so-called thermal stresses (TS) evolve after the deposition due to the mismatch between the coefficient of thermal expansion (CTE) for coating and substrate, which might be compressive or tensile depending on that mismatch (Ref 22). For thin coatings, this is given by

$$\sigma_{th} = \frac{E_c}{1 - \nu_c} (\alpha_c - \alpha_s) (T_s - T_0) \quad (\text{Eq 2})$$

In addition to the previous equation, α_s represents the CTE of the substrate, and T_0 represents the room temperature (Ref 20).

For estimating the peening stresses, there are a great number of influencing parameters, e.g., the kind of contact makes it difficult to analytically model these residual stresses, which is, therefore, done using *Finite Element* (FE) models in general (Ref 25–27). Another approach is the modeling of residual stresses for shot peening, which is

a related process due to the impact of solid particles in CGS (Ref 26, 28). Further analytical models like the one from Tsui et al. are widely used in the literature for estimating the uniform residual stress in coatings (Ref 20, 29).

The residual stress levels in coatings are often measured using diffraction or hole drilling methods (Ref 18, 19, 23). In this paper, we will focus on curvature measurements as this method allows to investigate the build-up of stresses during the whole spraying process. This is done by the so-called ICP sensor, which measures the curvature during the spray process. The curvature investigations of the residual stress state in thermal spray processes using the in situ curvature measurement via ICP sensor are commonly done for APS or HVOF techniques (Ref 21, 23, 30) with only a little scope for CGS applications, as done by Suhonen et al. (Ref 4) or Lett et al. (Ref 31).

For calculating the residual stress from the curvature, Stoney's equation is used (Ref 32):

$$\sigma_{\text{St}} = \frac{E'_s t_s^2}{6 t_c} \kappa \quad (\text{Eq 3})$$

where σ is the calculated residual stress, $\kappa = 1/R$ as the linearized curvature over the coating passes (R radius of curvature), E'_s , t_s , E'_c , and t_c are the in-plane elastic modulus ($E' = E/(1 - \nu)$) and thickness of substrate and coating, respectively. While Stoney's equation is widely used for the stress development in very thin films, it may cause errors for thickness ratios of $t_c/t_s \geq 0.1$ as the Young's modulus of the coating is neglected (Ref 33) but offers a simple approach to evaluate the residual stress for thermally sprayed coatings. In the literature, there are modifications for thicker coatings, also considering the Young's modulus of the coating such as Atkinson (Ref 34), Brenner–Senderoff (Ref 35), or Benabdi (Ref 36). It should be noted that the ICP sensor measures stress by their release into deformation. If large deformation is permitted (e.g., by substrate plasticity), the stress field is redistributed accordingly. Thus, it is desirable to limit the deformation by using a thick substrate (but thin enough to have a good curvature signal).

In this paper, IN718 is used as a coating material. This alloy is a frequently used material for high-temperature components especially in gas turbines. Due to the harsh environment, parts of these components are often damaged and have to be restored. Cold gas spraying has been established as a promising process to repair such components. Often, it is advantageous to restore also thicker volumes. Especially in these structures, existing high compressive stress levels might lead to large energy release rates promoting spallation. Hence, the aim of the present investigation was to find a possible way to adjust stress levels in cold spray coatings.

Experimental Procedures

Sample Preparation

For the coating, an IN718 powder (Oerlikon-Metco, Troy, MI, USA) with spherical morphology and mean size diameter of $d_{50} = 14 \mu\text{m}$ without pre-treatment was used. A more detailed investigation is given in Singh et al. (Ref 37). The powder is subject of a patent application filed by Oerlikon. It contains a significant amount of additional nickel–aluminum, which is claimed to ensure a dense and good adhering coating due this blended phase (Ref 18, 38). That feedstock powder was deposited on solution heat-treated IN718 substrates and 316 stainless steel specimens with dimensions of $228.0 \text{ mm} \times 25.4 \text{ mm}$ at several thicknesses (Table 2). Prior to the curvature measurements, no pre-treatment was done.

The used cold spray facility was an Impact 5/11 system (Impact Innovations GmbH, Germany) with a water-cooled D24 de-Laval type converging–diverging nozzle and nitrogen as propellant gas. Inlet gas temperature and pressure were 950°C and 4 MPa , respectively. About 60 mm was chosen as standoff distance between nozzle exit and substrate surface with the spray angle of 90° . As meander, 1 mm was used.

The coating thickness was kept constant for a varying robot traverse speed. Therefore, the number of passes and powder feed rate in the powder hopper had to be adjusted. Two conveyor disks were used for the Impact Powder Feeder. Since low and precise powder feed rates are required for the lowest mass flow rate, the disk with the double number of drill holes at half the size is recommended. The parameter conditions are listed in Table 1. In the following, condition no. 1 for 500 mm/s will also be called “Standard.”

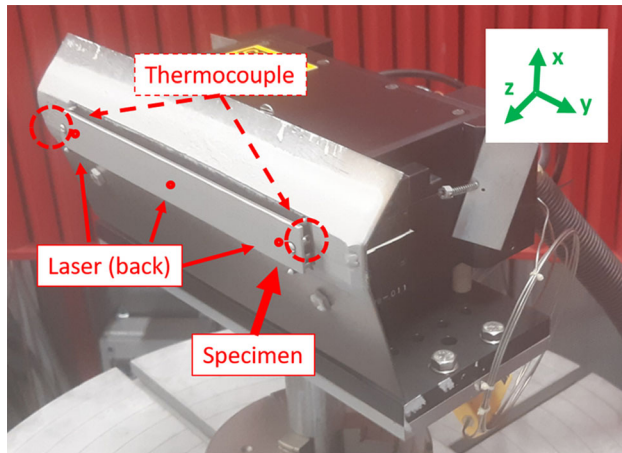
In Situ Curvature Measurement

The curvature during and after deposition was recorded using the in situ coating properties sensor (ICP sensor) from *Reliacoat Technologies LCC* (East Setauket, USA). In this in situ curvature device, the bending specimen is fixed on both sides to the supports using spring elements without constraining the curvature. The displacement of the specimen during the stress build-up of the deposition process is monitored by three lasers and simultaneously converted into the corresponding curvature. The complete setup is shown in Fig. 1.

In addition to the temperature measurement via two thermocouples at both supports, the local temperature on the substrate surface was acquired using a pyrometer type 3MH1 (Optris GmbH, Germany) focused on the center of

Table 1 Parameter conditions for robot traverse speed, number of passes, and powder feed rate

Condition, –	Robot traverse speed, mm s ⁻¹	Passes, –	Mass feed rate, g min ⁻¹
1	500	8	24.09
2	250	8	12.05
3	250	4	24.09
4	125	8	6.02
5	62.5	4	6.02

**Fig. 1** Setup for the ICP sensor including the specimen (red, bold), two thermocouples (red, dashed), and three lasers (red) on the rear side. A schematic representation is given by Mutter et al. (Ref 23). Directions are given in green as length (y-direction), width (x-direction), and normal (z-direction). The curvature was analyzed in y-direction

the substrate. During and after the deposition, the displacement with corresponding curvature and temperature is simultaneously monitored. The final residual stress state is calculated from the superposition of deposition stresses (DS) arising during the spraying and thermal stresses occurring after the spraying. The properties for powder and substrate material are given in Table 2.

Characterization Methods

To evaluate the deposition efficiency (DE), every specimen is weighted before and after the deposition. The thickness of substrate and the as-sprayed specimens were evaluated by using a micrometer screw. Measurement of the Vickers hardness was done on 10 points along the specimen with an applied load of 500 g using Duramin A300 (Struers GmbH, Germany).

In addition to the in situ curvature measurement, the post-deposition curvature was analyzed using an optical profilometer with a P-CHR-10000 sensor (Model CT350T, cyberTECHNOLOGIES GmbH, Germany). This setup was also used for validating the flatness of the substrates before deposition. Roughness measurements of all coatings were

Table 2 Properties for biaxial Young's modulus and Poisson ratio for IN718 (substrate and powder) and stainless steel (Ref 19). Thickness was measured via micrometer screw. Vickers hardness was evaluated using a weight of 0.5 kg. Powder hardness is referred to the as-sprayed state and was measured on a cross-section of the coating

Material	<i>E</i> , GPa	<i>ν</i> , –	Hardness, HV 0.5	Thickness, mm
IN718 powder	180	0.29	520	...
IN718 substrate	200	0.29	240	1.6 and 3.2
Stainless steel	200	0.30	150	1.3

carried out using the same device with a P-CHR-1000 on an area of $20 \times 20 \text{ mm}^2$.

For investigating the microstructure, the following procedure was performed: Sectioning the coated specimen “in-plane” and “out-of-plane” relative to the spray meander direction via Discotom-100 (Struers GmbH, Germany), grinding and polishing until the final step using the ATM Saphir 550 (Struers GmbH, Germany). A scanning electron microscope Zeiss GeminiSEM450 (Zeiss, Oberkochen, Germany) was used for microstructure observation of the polished cross-section.

Results and Discussion

Preliminary Experiments

As already mentioned, the ICP sensor monitors the displacement during the deposition and transfers it to the corresponding curvature. The ICP measurement for the spraying process using standard conditions for the deposition of IN718 powder on IN718 substrates with thickness (t_s) of 1.6 mm is shown in Fig. 2(a). The raw data from the ICP sensor for displacement d , curvature κ , and substrate temperature on the rear side T_s are monitored over time. This experiment includes three preheating passes ($0 \text{ s} < t < 100 \text{ s}$), eight coating passes ($100 \text{ s} < t < 400 \text{ s}$), and the cooling period ($> 400 \text{ s}$) until room temperature is reached. Each deposition pass ($\sim 30 \text{ s}$) is marked as pinnacle-shaped peak. All coatings, deposited with the conditions given in Table 1 including the just presented thin

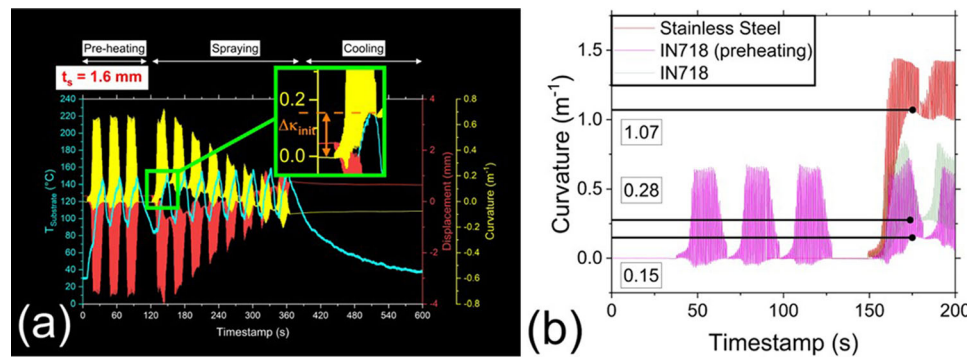


Fig. 2 Results of ICP sensor data monitoring the substrate curvature κ (yellow), displacement d (red), and substrate temperature T_s (blue) during the deposition of an IN718 coating on IN718 substrate. Thin IN718 substrate ($t_s = 1.6 \text{ mm}$, a) has been used at a robot traverse speed of 500 mm/s and the given conditions in Table 1, resulting in a coating thickness around 730 μm . The initial curvature (orange) of

$\kappa_{\text{init}} = 0.15 \text{ m}^{-1}$ is highlighted orange for the first deposition layer in the higher magnification (light green). Preliminary studies focused on the first deposition pass (b) revealed an influence of stainless steel ($t_s = 1.3$, red), IN718 (pale green), and IN718 + three preheating cycles (purple) used as substrate material

substrate, have similar thicknesses of about $730 \pm 15 \mu\text{m}$ and roughness values of $R_z = 6.5 \pm 0.5 \mu\text{m}$. The DE is consistently about 80%. An initial positive curvature of about $\kappa_{\text{init}} = 0.15 \text{ m}^{-1}$ develops during the first deposition pass ($120 \text{ s} < t < 150 \text{ s}$) in Fig. 2(a). This positive initial curvature suggests tensile residual stress in the first place, which decreases with each subsequent deposition cycle until a negative curvature is reached ($\kappa = -0.1 \text{ m}^{-1}$). The positive displacement and thus negative curvature indicate the dominant compressive residual stresses in CGS. These might result from an increased peening effect from the particle impact with each subsequent layer. In general, a huge variation (in the following called “noise”) during each pass can be identified related to the high-velocity gas jet causing deflections of several millimeters to the substrate ($\Delta d_{\text{thin}} > 3 \text{ mm}$). This might be critical for in situ curvature measurements in cold spray processes, since this deflection is superimposed to the one from residual stresses (Ref 4, 23). The amount of deflection due to the gas decreases with increasing layer thickness. This can be explained by the higher thickness of the sample (from 1.6 to 2.33 mm) and hence the increasing stiffness. The curvature for a constant force should follow a linear dependence.

With respect to the initial shift in curvature, the overall stress during the deposition is calculated by inserting the linearized curvature change from first to last deposition cycle ($\Delta\kappa_{\text{dep}} = -0.25 \text{ m}^{-1}$) into Stoney’s equation (Eq 3). By proceeding in the same way with the linearized curvature change after the last deposition cycle until room temperature is reached ($\Delta\kappa_{\text{cool}} \sim -0.015 \text{ m}^{-1}$), the residual stress is calculated as the sum of the so-called deposition stresses (DS) and thermal stresses (TS) during the cooling period. As substrate and coating material are the same, only a small change in curvature during the

cooling period is expected. The ICP data confirms this issue since a neglectable curvature change was observed compared to the total evolving curvature. For that reason, it can be claimed that the final residual stress state primary results from the stresses arising during deposition.

The previous studies and pre-trials shown in Fig. 2(b) revealed a significant influence of the first particle impact, possibly causing a curvature by particle–substrate interaction whose curvature is then incorrectly interpreted in the stress calculation as deposition stress (Ref 4). Furthermore, the deposition on an already “pre-bended” substrate might affect the related stress evolution. Stainless steel substrates with $t_s = 1.3 \text{ mm}$, coated with IN718 powder at standard conditions (see Table 1), showed a large initial curvature of about $\kappa_{\text{init}} = 1.07 \text{ m}^{-1}$. It should be pointed out that the maximum deflection due to contact of sensor and substrate rear side was reached at a curvature of $\kappa_{\text{max}} = 1.5 \text{ m}^{-1}$, indicated by the flat lines at this curvature. By using IN718 substrates with $t_s = 1.6 \text{ mm}$, the initial curvature decreased significantly to $\kappa_{\text{init}} = 0.28 \text{ m}^{-1}$ with no contact to the sensor. Concerning the different hardness of the substrate materials (s. Table 2), the impact of solid IN718 particles on a significantly softer material might lead to an increased penetration of the substrate compared to the combination of equal materials, possibly causing an enhanced deflection due to the first impact. After depositing the first layer, the hardness of particle and first layer can be approximated nearly the same with a consecutive trend of decreasing curvature. This finding and the huge deflection from the gas jet, especially for the slightly thinner stainless steel substrates, indicate a strong influence of the substrate and coating material on the final residual stress state for ICP measurement.

Sun et al. reported an improved adhesion of IN718 powder particles on IN718 substrate up to a certain

temperature by considering the substrate temperature before spraying (Ref 39). Therefore, three preheating cycles (the gas jet heats the substrate surface without particle impinging) have been added prior to the deposition process. As an additional effect, a further decrease in initial curvature could be achieved for adding these three preheating cycles ($\kappa_{\text{init}} = 0.15 \text{ m}^{-1}$ in Fig. 2b). It can be noted that the preheating itself did not introduce a permanent curvature of the substrate before the actual coating process. Based on this preliminary tests, IN718 substrates including preheating were chosen for the following experiments.

Effect of Variable Robot Speed on Curvature Measurement

The arising residual stress state in CGS mainly depends on the condition of the impacting particles (peening stresses) on the substrate as well as the interaction of coating and substrate during deposition and the cooling period (quenching + thermal stresses). Thermal stresses should be approximately zero due to the combination of similar materials. Peening stresses are known to be compressive and dominant in CGS, while the effect of typically tensile quenching stresses depends on the status of the particles. Since hot particles have a better bonding, according to the ASI model, and high-velocity particles increase the peening effect, initial gas temperature and pressure were shifted in another study by Lang et al. (Ref 40) to adjust the primary compressive residual stress state of cold-sprayed coatings with respect to the limits of the cold spray facility. These experiments on slightly higher gas temperature and a relatively lower gas pressure led to an impact of particles at higher temperatures and lower velocities. Residual stress analysis with neutron diffraction revealed a slightly reduced compressive residual stress state. Based on these findings, an extension of this condition could further reduce the compressive residual stresses. On the other hand, the maximum boundaries of the CGS facility are almost reached. In addition, a further increase in gas temperature could lead to clogging in the nozzle, especially for small particles, and therefore negative effects to the deposition process. One possibility to increase induced heat is a decreasing standoff distance, which might affect the DE and bow shock phenomena and is, therefore, excluded in this study (Ref 14, 15). Another option is a shift in robot traverse speed, where a slower crossing speed should increase the amount of heat induced at the impact zone (Ref 41). Based on the findings for the preheating, the impact of solid particles on thermally softened material should decrease the dominant PS in cold spray.

Therefore, experiments on doubled IN718 substrate thickness ($t_s = 3.2 \text{ mm}$) on variable robot traverse speed for the conditions given in Table 1 were carried out. To

match the expected change in substrate temperature, the number of preheating cycles has been adjusted to the specific robot traverse speed. Nevertheless, these were chosen in a way to keep the parameters in proportion for a constant coating thickness. Figure 3 shows the highest (500 mm/s) and lowest (62.5 mm/s) robot speed used in these trials. For the standard conditions in Fig. 3(a), the substrate temperature revealed the same extent as in Fig. 2(a). The noise was significantly reduced, while the neglectable small curvature after the preheating ($\Delta\kappa_{\text{pre}} \sim -0.005 \text{ m}^{-1}$) is in good agreement to the pre-experiments with thinner substrate. The first coating pass only led to a marginal initial curvature change ($\Delta\kappa_{\text{init}} = -0.007 \text{ m}^{-1}$), while the following deposition cycles resulted again in a continuous negative decrease in curvature, implying compressive residual stresses due to peening effects. Another similarity is the slight change in curvature during cooling, representing only a small variation in thermal stresses.

In comparison with the results for the standard conditions, experiments on the lowest robot traverse speed of 62.5 mm/s in Fig. 3(b) demonstrate an opposite curvature of the specimen. The curvature now tends to be positive, suggesting a tensile stress state in this cold-sprayed coating. Both findings from the ICP sensor fit to the smooth circle-shaped curvature of the specimen and its corresponding contour plot as shown in Fig. 3(c), (d), (e), and (f). The substrate temperature now tends to be significant higher with decreasing robot velocities, see Table 3. A permanent displacement after the single preheating cycle can be detected ($\Delta\kappa_{\text{pre}} \sim 0.04 \text{ m}^{-1}$), which is followed by a noticeable initial curvature change ($\Delta\kappa_{\text{init}} = 0.1 \text{ m}^{-1}$) after the first deposition cycle and an increase in curvature with each subsequent layer.

The calculated residual stresses using Stoney's equation Eq 3 are presented in Fig. 4. In general, a decline of the stress with decreasing robot speed is visible for these conditions. Starting at compressive residual stresses at the highest robot traverse speed, the stress state becomes roughly zero at about 250 mm/s. A further reduction of the robot traverse speed led to an increase in tensile residual stresses as well as an increased substrate temperature as shown in Table 4. Measurement of the post-curvature after removing the specimen from the ICP sensor, using the optical profilometer, confirms the in-situ results.

This higher substrate temperature at slow speed corresponds to an increased temperature at the impact zone compared to the mean substrate temperature and is caused by the longer residence time of the gas jet on the same position as shown by Lin et al. (Ref 42). Within the scope of convective heat transfer, this moving heat source might induce more heat to the impact zone without the possibility to fully dissipate and thus support the bonding process in

Fig. 3 Curvature κ (yellow), displacement d (red), and substrate temperature T_s (blue) for $v_r = 500$ mm/s (a) and $v_r = 62.5$ mm/s (b) on IN718 substrate with $t_s = 3.2$ mm. The standard conditions lead to the expected compressive residual stresses, while the slowest robot speed shows tensile residual stresses. The 2D contour plots of topography as well as images of the coated specimen are in good agreement to the positive (compressive, c + e) and negative displacement (tensile, d + f). See Fig. 1 for directions of the contour plot (Color figure online)

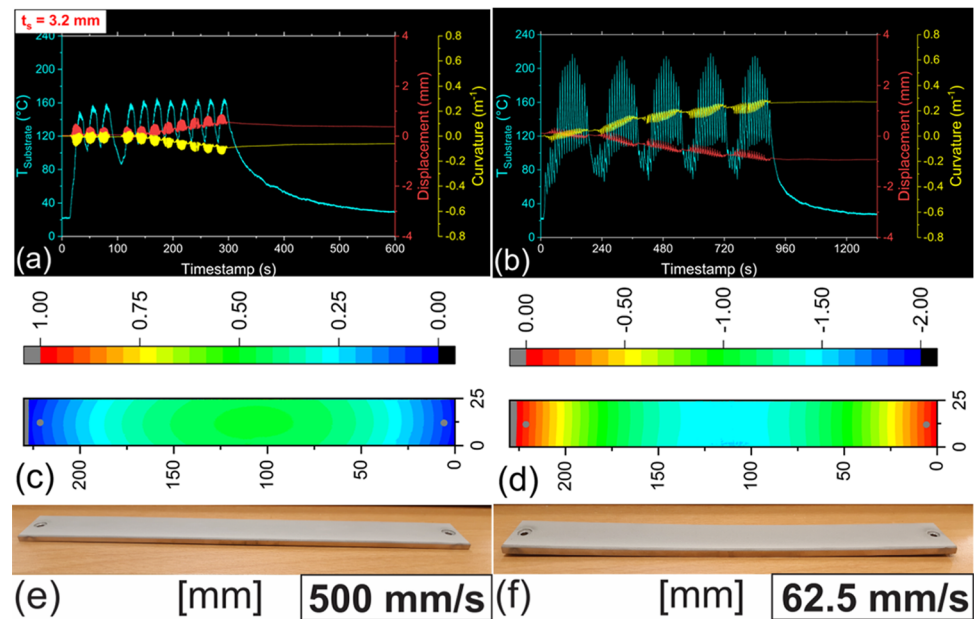


Table 3 Residual stress from in situ curvature ($\sigma_{res,ICP}$), optically measured curvature ($\sigma_{res,optical}$), and the model ($\sigma_{res,Model}$) with corresponding surface temperature ($T_{s,max}$, pyrometer), temperature at the thermocouples on the rear side (T_{th}), and coating thickness (t_c)

Condition, –	$\sigma_{res,ICP}$, MPa	$\sigma_{res,optical}$, MPa	$\sigma_{res,Model}$, MPa	$T_{s,max}$, K	T_{th} , K	T_{loc} , K	t_c , mm
1	– 35.1	– 43.67	– 23.77	593.15	403.15	460.71	0.760
2	10.8	8.11	– 18.36	633.15	413.15	469.94	0.755
3	96.9	101.04	61.98	663.15	413.15	488.29	0.716
4	73.2	74.80	20.46	703.15	423.15	485.96	0.767
5	140.8	162.28	127.39	773.15	433.15	516.58	0.715

CGS following the ASI model from Assadi et al. (Ref 7). Particles are deposited on this hot substrate region which cools down after the gas stream moved further. For the thermally softened substrate, caused by the higher local temperature, a lower peening effect from the particle impact is expected and demonstrated for simulated single-particle impacts by Oviedo et al. (Ref 43). On the other hand, the tensile residual stress increases with the local substrate temperature, which is in good agreement with similar studies (Ref 31, 41). In the literature, these arising tensile stresses are referred to an quenching effect of the particles, comparable to the high-temperature thermal spray processes (Ref 41). Since the particles are not expected to melt and the particle temperature does not vary for a modified robot traverse speed (the gas velocity/temperature itself does not change), this quenching effect might be related to the thermal contraction due to the cooldown of hot coating to the average temperature on the cold substrate during the deposition period. Since the difference in CTE between substrate and coating is neglectable, see cooling periods in Fig. 3, these thermal stresses

during the deposition, called thermal deposition stresses (TDS) from here on, mainly arise from the temperature gradient between hot and cold layers.

No differences in microstructure could be found for 500 mm/s and 62.5 mm/s (see Fig. 5). The shown cross-sections are given representatively for both orientations without any discrepancies. The additional experiment in Fig. 4 for condition 3 with twice the powder feed rate and half the number of passes at 250 mm/s reveals even higher tensile residual stresses. This significant increase in residual stresses with the powder feed rate has also been reported for HVOF spraying process by Shinoda et al. (Ref 30). According to the findings from this study, the superposition of longer residence time of the gas jet and the higher particle density at the impact zone results in an even higher local temperature at the impact zone compared to the experiment on half the feed rate (see Table 3). Combined with the previous assumptions, the higher tensile residual stresses are related to this increased local heating of the substrate due to the additional heat source from the impacting particles.

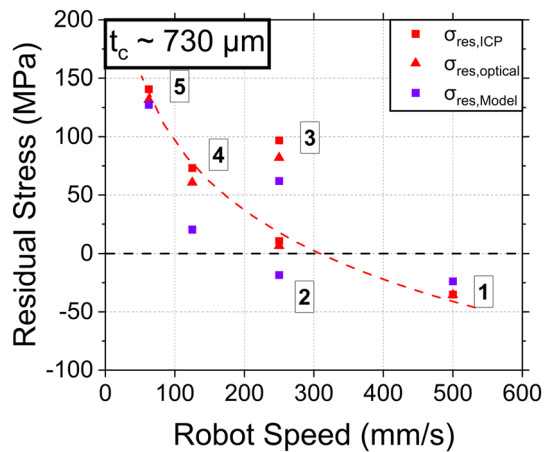


Fig. 4 Residual stress values resulting from in situ curvature (red squares) and the respective optically measured curvature (red triangles) for a decreasing robot traverse speed and the conditions in Table 1. The conditions by means of the red dashed trendline (no. 1, 2, 4, and 5) were adjusted to achieve the same coating thickness in relatively constant ratio for each parameter. An additional experiment for a doubled powder feed rate (no. 3, away from the dashed trendline) revealed even higher tensile residual stresses. The residual stresses determined by the model (purple squares) are in good agreement with the experimental results

Comparison of Analytical Model and Experiments

In order to analyze whether the presented thoughts of the previous section can explain the observed residual stress dependence on both robot speed and deposition rate, a simplified analytical model was developed for calculating the residual stress state. Heat transfer between a moving

source and the substrate has been modeled for cold gas spray (Ref 42), laser and welding applications (Ref 44, 45), but the heat transfer of the impacting particles was not taken into account for cold gas spray. As mentioned already, the two main factors contributing to the final stress state are peening (compressive) and thermal deposition (tensile) effects. The model uses an estimated value for the peening stresses based on the literature (Ref 19, 40), while the TDS can be derived from the arising temperature gradient between coating and substrate (see Eq 1).

The dominant impingement (Ref 4) of a hot gas jet loaded with heated particles (heat source) causes a heat transfer to the substrate (heat sink). The resulting heat balance at the impact zone is determined by the temperature level and the amount of emitted or absorbed heat. Heat radiation was neglected for this analytical solution. For the interaction between the gas stream and the substrate, a convective heat transfer was assumed (see Eq 4). Heat transfer between the deposited particles and the substrate depends on the difference between the particle temperature and the local temperature (see Eq 5). Solid-state conduction is taken for the substrate following Fourier's law. The governing equations for each contributing heat input are, therefore, derived as follows:

$$\dot{q}_g = h_g (T_g - T_{loc}) \quad (\text{Eq 4})$$

$$\dot{q}_p = \beta (T_p - T_{loc}) \quad (\text{Eq 5})$$

$$\dot{q}_s = \frac{\lambda_s}{d_{diff}} (T_{loc} - T_s) \quad (\text{Eq 6})$$

Table 4 Data used for the analytical model based on previous experiments and the KSS software (Ref 6, 12, 46, 47)

b , m	c_p , J kg ⁻¹ K ⁻¹	D_u , m	h_g , W m ⁻² K ⁻¹	T_g , K	T_p , K	ρ_c , kg m ⁻³	λ_s , W m ⁻¹ K ⁻¹	σ_c , K ⁻¹
0.001	435	0.008	1200	1000	740	8000	10	13×10^{-6}

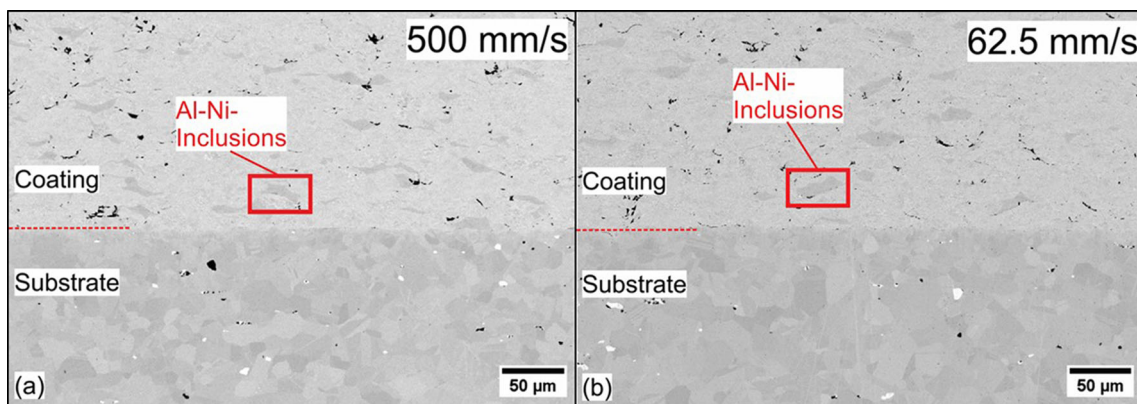


Fig. 5 SEM analysis of the samples prepared with 500 mm/s (a) and 62.5 mm/s (b) robot speed revealed the same microstructure. The cross-sections for both specimens show no differences to previous investigations using the same materials (Ref 18, 37). A good adhesion

at the interface is visible, separating the substrate and coating with scattered pores entailing Al-Ni-enriched inclusions at an overall low porosity

where \dot{q} is the heat flux for gas (g), particles (p), and substrate (s), respectively. The same term is used for the temperatures T_x , T_{loc} is the local temperature after the particle impact. This temperature is determined via the thermocouples on the rear side of the sample. Further abbreviations are the heat transfer coefficient of the gas (h_g), the thermal conductivity of the substrate (λ_s), the diffusion length (d_{diff}), and β which is used to describe the heat transfer from the particles (see below).

The heat transport within the substrate can be estimated with the well-known equation for the diffusion length, see Eq 7, in which the diffusion length is proportional to the square root of thermal diffusion coefficient D_{diff} and the time scale for heat diffusion process τ_{diff} . The latter is the quotient of robot traverse speed crossing the area of the gas spot d_u , whose diameter is taken as 8 mm for the nozzle in use, based on the previous experiment.

$$d_{diff} \sim 2\sqrt{D_{diff}\tau_{diff}} \quad (\text{Eq 7})$$

$$D_{diff} = \frac{\lambda_s}{\rho_s c_{p,s}} \quad (\text{Eq 8})$$

$$e = \sqrt{\lambda_s \rho_s c_{p,s}} \quad (\text{Eq 9})$$

$$T_{loc} = \frac{h_g T_g + \beta T_p + \frac{e}{2\sqrt{\tau_{diff}}} T_s}{h_g + \beta + \frac{e}{2\sqrt{\tau_{diff}}}} \quad (\text{Eq 10})$$

Since the heat flux into the substrate is balanced with the heat flux of the gas stream and the impacting particle, the sum of Eqs 4 and 5 are equal to Eq 6. Inserting the thermal effusivity e (Eq 9) leads to an equation for the local surface temperature T_{loc} (Eq 10).

As the first step for estimating the heat transferred by the particles, the stored energy of the coating β_{en} can be directly calculated from material properties and measured data (Eq 11). The temperature distribution around the spot is hard to determine and would need simulation support, e.g., ANSYS or ABAQUS. Therefore, the area of the spray spot is taken as volume element including the subsequent layer thickness t_c . Considering the energy deposited per layer, the introduced heat additionally depends on the number of passes z , the spray spot diameter d_u , the width of the spraying meander b , and the robot traverse speed v_r (see Eq 12):

$$\beta_{en} = \rho_c c_{p,c} t_c \quad (\text{Eq 11})$$

$$\beta = \frac{\rho_c c_{p,c} t_c}{\frac{d_u}{b} z \frac{d_u}{v_r}} = \frac{\rho_c c_{p,c} b}{d_u^2} * \frac{v_r t_c}{z} \quad (\text{Eq 12})$$

$$\beta_0 = \frac{\rho_c c_{p,c} b}{d_u^2} \quad (\text{Eq 13})$$

β_0 in Eq 13 is a pre-factor.

Inserting the calculated local temperature and the substrate temperature into Eq 1, considering E'_c instead of E_c

and replacing T_m by T_{loc} , results in the thermal deposition stress σ_{TDS} due to the local temperature difference at the impact zone. The average amount of peening stresses σ_p introduced by the impacting particles was set to -270 MPa, which is in good agreement to the previous studies using the same materials (Ref 19, 40). This value was taken as constant over each robot traverse speed.

$$\sigma_{res,Model} = \sigma_p + \sigma_{TDS} \quad (\text{Eq 14})$$

It is clearly visible in Fig. 4 that the trend for the curvature experiments and the model is in good agreement with each other with the exception of a discrepancy at 125 mm/s. So, the presented analytical model can at least semi-quantitatively explain the observed findings from the ICP sensor. These are in good agreement to the re-calculated residual stresses with the analytical model, including the particle heat flux. Additionally, the constant value of -270 MPa seems to be a good indicator for the compressive residual stresses in the coating deposited under given conditions. Hence, it verified the approach to use an average value from a through-thickness stress measurement. As the model does not consider the softening of the material due to the higher substrate temperature T_{loc} , and therefore decreasing peening stresses, it might be concluded that this effect is probably neglectable.

It was observed that a definite residual stress state in cold-sprayed coatings could be adjusted by variation of adequate deposition parameters, in this study by changing robot traverse speed and powder feed rate. Measurement by using the ICP sensor did not cause any problems in cold spray related to the high-velocity gas jet. Substrates with a thickness of 3 mm were used to reduce the deflection of the specimen caused by the gas stream (potential artefact in the measurement), which allowed for more reliable and consistent collection of data using the ICP sensor. This also reduced the initial impact peak and caused small deflection, which might be critical for the analysis. Additionally, the robot traverse direction and the meander width as done by Lett et al. (Ref 31) might be considered as influencing variables for the local temperature with respect to the layer thickness per pass for reasons of comparability. In addition to the varied robot traverse speed, experimental investigations on the number of powder particles per deposition pass are a promising approach for an adjustment of residual stresses.

Conclusions

This study demonstrated the opportunity of adjusting a certain residual stress state in CGS by varying the robot traverse speed and powder feed rate. Comparison of cross-sections for the maximal and minimal robot traverse speed

revealed a similar state of dense coatings. The main findings can be concluded as follows:

1. The in situ curvature during the deposition has been successfully evaluated using the ICP sensor for IN718 coatings on IN718 substrate. The high-velocity gas jet did not cause problems for the measurement or the sensor. By slowing down the robot traverse speed, the typical compressive residual stresses could be shifted to tensile residual stresses. An increased local temperature at the particle impact zone was identified. This may lead to tensile residual stresses for cold-sprayed coatings.
2. Post-deposition curvature showed a good accordance with the in situ curvature measured by the ICP sensor. Depending on the robot traverse speed, a specific ratio of generally compressive peening stresses and generally tensile thermal deposition stresses during the deposition period has been formed, where the latter revealed to be dominant for the final residual stress state. Thermal stress during the cooling period was negligible.
3. In addition to the robot traverse speed, a significant effect of the powder feed rate on the final residual stress state has been revealed. The combination of a longer gas jet residence time and an increased number of particles at the gas spot might increase the local temperature even further and enhance the local temperature gradient leading to higher tensile stresses.
4. An analytical model was developed which described the residual stress development as a result of the local temperature increases during deposition. The model revealed results for the final residual stress state which were in good agreement with the measurements of the ICP sensor.

Acknowledgments The authors acknowledge the financial support by the German Research Foundation (DFG) under Grant Number VA163/11-1 and the German Federal Ministry of Economics and Climate Protection under Grant Number 20T1703C. Special thanks to Mr. Karl-Heinz Rauwald for his help to operate the cold gas facility. The authors would also like to express their thanks to Dr. Doris Sebold for SEM imaging.

Funding Open Access funding enabled and organized by Projekt DEAL.

Open Access This article is licensed under a Creative Commons Attribution 4.0 International License, which permits use, sharing, adaptation, distribution and reproduction in any medium or format, as long as you give appropriate credit to the original author(s) and the source, provide a link to the Creative Commons licence, and indicate if changes were made. The images or other third party material in this article are included in the article's Creative Commons licence, unless indicated otherwise in a

credit line to the material. If material is not included in the article's Creative Commons licence and your intended use is not permitted by statutory regulation or exceeds the permitted use, you will need to obtain permission directly from the copyright holder. To view a copy of this licence, visit <http://creativecommons.org/licenses/by/4.0/>.

References

1. A.P. Alkhimov, A.N. Papyrin, V.F. Kosarev, and N.I. Nesterovic, Gas-Dynamic Spraying Method for Applying a Coating (Novosibirsk), n.d.
2. M.B. Henderson, D. Arrell, R. Larsson, M. Heobel, and G. Marchant, Nickel Based Superalloy Welding Practices for Industrial Gas Turbine Applications, *Sci. Technol. Weld. Join.*, 2004, **9**(1), p 13–21.
3. T. Petrat, B. Graf, A. Gumenyuk, and M. Rethmeier, Laser Metal Deposition as Repair Technology for a Gas Turbine Burner Made of Inconel 718, *Phys. Procedia*, 2016, **83**, p 761–768.
4. T. Suhonen, T. Varis, S. Dosta, M. Torrell, and J.M. Guilemany, Residual Stress Development in Cold Sprayed Al, Cu and Ti Coatings, *Acta Mater.*, 2013, **61**(17), p 6329–6337.
5. K. Pallos, Gas Turbine Repair Technology, *Atlanta GA USA GE Energy Serv. Technol. GE Power Syst.*, 2001.
6. A.S. Agazhanov, D.A. Samoshkin, and Y.M. Kozlovskii, Thermophysical Properties of Inconel 718 Alloy, *J. Phys. Conf. Ser.*, 2019, **1382**(1), p 012175.
7. H. Assadi, F. Gärtner, T. Stoltenhoff, and H. Kreye, Bonding Mechanism in Cold Gas Spraying, *Acta Mater.*, 2003, **51**(15), p 4379–4394.
8. M. Grujicic, C.L. Zhao, W.S. DeRosset, and D. Helfritsch, Adiabatic Shear Instability Based Mechanism for Particles/Substrate Bonding in the Cold-Gas Dynamic-Spray Process, *Mater. Des.*, 2004, **25**(8), p 681–688.
9. M. Hassani-Gangaraj, D. Veyssset, V.K. Champagne, K.A. Nelson, and C.A. Schuh, Adiabatic Shear Instability is not Necessary for Adhesion in Cold Spray, *Acta Mater.*, 2018, **158**, p 430–439.
10. T. Hussain, D.G. McCartney, P.H. Shipway, and D. Zhang, Bonding Mechanisms in Cold Spraying: The Contributions of Metallurgical and Mechanical Components, *J. Therm. Spray Technol.*, 2009, **18**(3), p 364–379.
11. V.K. Champagne, D. Helfritsch, P. Leyman, S. Grendahl, and B. Klotz, Interface Material Mixing Formed by the Deposition of Copper on Aluminum by Means of the Cold Spray Process, *J. Therm. Spray Technol.*, 2005, **14**(3), p 330–334.
12. T. Schmidt, F. Gärtner, H. Assadi, and H. Kreye, Development of a Generalized Parameter Window for Cold Spray Deposition, *Acta Mater.*, 2006, **54**(3), p 729–742.
13. H. Assadi, H. Kreye, F. Gärtner, and T. Klassen, Cold Spraying—A Materials Perspective, *Acta Mater.*, 2016, **116**, p 382–407.
14. J. Pattison, S. Celotto, A. Khan, and W. O'Neill, Standoff Distance and Bow Shock Phenomena in the Cold Spray Process, *Surf. Coat. Technol.*, 2008, **202**(8), p 1443–1454.
15. W.-Y. Li, C. Zhang, X.P. Guo, G. Zhang, H.L. Liao, C.-J. Li, and C. Coddet, Effect of Standoff Distance on Coating Deposition Characteristics in Cold Spraying, *Mater. Des.*, 2008, **29**(2), p 297–304.
16. C.-J. Li, W.-Y. Li, Y.-Y. Wang, and H. Fukunuma, in *Effect of Spray Angle on Deposition Characteristics in Cold Spraying*, ed. by B.R. Marple and C. Moreau (Orlando, Florida, USA, 2003), p 91–96. <https://doi.org/10.31399/asm.cp.itsc2003p0091>.

17. J. Fiebig, E. Bakan, T. Kalfhaus, G. Mauer, O. Guillon, and R. Vaßen, Thermal Spray Processes for the Repair of Gas Turbine Components, *Adv. Eng. Mater.*, 2020, **22**(6), p 1901237.
18. R. Vaßen, J. Fiebig, T. Kalfhaus, J. Gibmeier, A. Kostka, and S. Schröder, Correlation of Microstructure and Properties of Cold Gas Sprayed INCONEL 718 Coatings, *J. Therm. Spray Technol.*, 2020, **29**(6), p 1455-1465.
19. R. Singh, S. Schrufer, S. Wilson, J. Gibmeier, and R. Vassen, Influence of Coating Thickness on Residual Stress and Adhesion-Strength of Cold-Sprayed Inconel 718 Coatings, *Surf. Coat. Technol.*, 2018, **350**, p 64-73.
20. T.W. Clyne, Residual Stresses in Surface Coatings and Their Effects on Interfacial Debonding, *Key Eng. Mater.*, 1995, **116-117**, p 307-330.
21. H. Ruiz-Luna, D. Lozano-Mandujano, J.M. Alvarado-Orozco, A. Valarezo, C.A. Poblano-Salas, L.G. Trápaga-Martínez, F.J. Espinoza-Beltrán, and J. Muñoz-Saldaña, Effect of HVOF Processing Parameters on the Properties of NiCoCrAlY Coatings by Design of Experiments, *J. Therm. Spray Technol.*, 2014, **23**(6), p 950-961.
22. A. Valarezo, W.B. Choi, W. Chi, A. Gouldstone, and S. Sampath, Process Control and Characterization of NiCr Coatings by HVOF-DJ2700 System: A Process Map Approach, *J. Therm. Spray Technol.*, 2010, **19**(5), p 852-865.
23. M. Mutter, G. Mauer, R. Mücke, R. Vaßen, H.C. Back, and J. Gibmeier, Investigations on the Initial Stress Evolution During Atmospheric Plasma Spraying of YSZ by In Situ Curvature Measurement, *J. Therm. Spray Technol.*, 2016, **25**(4), p 672-683.
24. T.W. Clyne and S.C. Gill, Residual Stresses in Thermal Spray Coatings and Their Effect on Interfacial Adhesion: A Review of Recent Work, *J. Therm. Spray Technol.*, 1996, **5**(4), p 401-418.
25. A. Fardan, C.C. Berndt, and R. Ahmed, Numerical Modelling of Particle Impact and Residual Stresses in Cold Sprayed Coatings: A Review, *Surf. Coat. Technol.*, 2021, **409**, p 126835.
26. J.K. Li, Y. Mei, and W. Duo, Mechanical Approach to the Residual Stress Field Induced by Shot Peening, n.d., p 7.
27. S. Guetta, M.H. Berger, F. Borit, V. Guipont, M. Jeandin, M. Boustie, Y. Ichikawa, K. Sakaguchi, and K. Ogawa, Influence of Particle Velocity on Adhesion of Cold-Sprayed Splats, *J. Therm. Spray Technol.*, 2009, **18**(3), p 331-342.
28. A.S. Franchim, V.S. de Campos, D.N. Travessa, and C. de Moura Neto, Analytical Modelling for Residual Stresses Produced by Shot Peening, *Mater. Des.*, 2009, **30**(5), p 1556-1560.
29. Y.C. Tsui and T.W. Clyne, An Analytical Model for Predicting Residual Stresses in Progressively Deposited Coatings Part 1: Planar Geometry, *Thin Solid Films*, 1997, **306**(1), p 23-33.
30. K. Shinoda, J. Colmenares-Angulo, A. Valarezo, and S. Sampath, Effect of Deposition Rate on the Stress Evolution of Plasma-Sprayed Yttria-Stabilized Zirconia, *J. Therm. Spray Technol.*, 2012, **21**(6), p 1224-1233.
31. S. Lett, A. Quet, S. Hémerly, J. Cormier, E. Meillot, and P. Villechaise, Residual Stresses Development During Cold Spraying of Ti-6Al-4V Combined with In Situ Shot Peening, *J. Therm. Spray Technol.*, 2022 <https://doi.org/10.1007/s11666-022-01514-w>
32. G.G. Stoney, The Tension of Metallic Films Deposited by Electrolysis, *Proc. R. Soc. Lond. Ser. Contain. Pap. Math. Phys. Charact.*, 1909, **82**(553), p 172-175.
33. C.A. Klein, How Accurate are Stoney's Equation and Recent Modifications, *J. Appl. Phys.*, 2000, **88**(9), p 5487-5489.
34. A. Atkinson, T. Johnson, A.H. Harker, and S.C. Jain, Film Edge-Induced Stress in Substrates and Finite Films, *Thin Solid Films*, 1996, **274**(1-2), p 106-112.
35. A. Brenner and S. Senderoff, Calculation of Stress in Electrodeposits from the Curvature of a Plated Strip, *J. Res. Natl. Bur. Stand.*, 1949, **42**(2), p 105.
36. M. Benabdi and A.A. Roche, Mechanical Properties of Thin and Thick Coatings Applied to Various Substrates. Part I. An Elastic Analysis of Residual Stresses within Coating Materials, *J. Adhes. Sci. Technol.*, 1997, **11**(2), p 281-299.
37. R. Singh, K.-H. Rauwald, E. Wessel, G. Mauer, S. Schrufer, A. Barth, S. Wilson, and R. Vassen, Effects of Substrate Roughness and Spray-Angle on Deposition Behavior of Cold-Sprayed Inconel 718, *Surf. Coat. Technol.*, 2017, **319**, p 249-259.
38. A.B.S. Wilson, M. Nestler, and S. Kudapa, Cold Gas Spray Coating Methods and Compositions, n.d.
39. W. Sun, A.W.Y. Tan, A. Bhowmik, I. Marinescu, X. Song, W. Zhai, F. Li, and E. Liu, Deposition Characteristics of Cold Sprayed Inconel 718 Particles on Inconel 718 Substrates with Different Surface Conditions, *Mater. Sci. Eng. A*, 2018, **720**, p 75-84.
40. F. Lang, J.-C. Schmitt, S. Cabeza, T. Pirling, J. Fiebig, R. Vassen, and J. Gibmeier, IN718 Cold Gas Repair Spray of Large Cavities—Microstructure and Residual Stresses, in *Proceedings of the 10th International Symposium on Superalloy 718 and Derivatives*, ed. by E.A. Ott, J. Andersson, C. Sudbrack, Z. Bi, K. Bockenstedt, I. Dempster, M. Fahrman, P. Jablonski, M. Kirka, X. Liu, D. Nagahama, T. Smith, M. Stockinger, and A. Wessman (Springer, Cham, 2023), p 739-753. https://doi.org/10.1007/978-3-031-27447-3_44.
41. D. Boruah, B. Ahmad, T.L. Lee, S. Kabra, A.K. Syed, P. McNutt, M. Doré, and X. Zhang, Evaluation of Residual Stresses Induced by Cold Spraying of Ti-6Al-4V on Ti-6Al-4V Substrates, *Surf. Coat. Technol.*, 2019, **374**, p 591-602.
42. E. Lin, I. Nault, O.C. Ozdemir, V.K. Champagne, A. Nardi, and S. Müftü, Thermo-mechanical Deformation History and the Residual Stress Distribution in Cold Spray, *J. Therm. Spray Technol.*, 2020, **29**(6), p 1424-1436.
43. F. Oviedo and A. Valarezo, Residual Stress in High-Velocity Impact Coatings: Parametric Finite Element Analysis Approach, *J. Therm. Spray Technol.*, 2020, **29**(6), p 1268-1288.
44. C.-K. Kim, An Analytical Solution to Heat Conduction with a Moving Heat Source, *J. Mech. Sci. Technol.*, 2011, **25**(4), p 895-899.
45. H. Yang, Z. Li, and S. Wang, The Analytical Prediction of Thermal Distribution and Defect Generation of Inconel 718 by Selective Laser Melting, *Appl. Sci.*, 2020, **10**(20), p 7300.
46. J.N. Sweet, E.P. Roth, and M. Moss, Thermal Conductivity of Inconel 718 and 304 Stainless Steel, *Int. J. Thermophys.*, 1987, **8**(5), p 593-606.
47. G. Mauer, R. Singh, K.-H. Rauwald, S. Schröder, S. Wilson, and R. Vaßen, Diagnostics of Cold-Sprayed Particle Velocities Approaching Critical Deposition Conditions, *J. Therm. Spray Technol.*, 2017, **26**(7), p 1423-1433.

Publisher's Note Springer Nature remains neutral with regard to jurisdictional claims in published maps and institutional affiliations.